

Evidence of linear and cubic Rashba effect in non-magnetic heterostructure

Sanchari Bhattacharya* and Sanjoy Datta†

Department of Physics and Astronomy,

National Institute of Technology, Rourkela, Odisha, India, 769008

The $\text{LaAlO}_3/\text{KTaO}_3$ system serves as a prototype to study the electronic properties that emerge as a result of spin-orbit coupling. In this article, we have used first-principles calculations to systematically study two types of defect-free (0 0 1) interfaces, which are termed as Type-I and Type-II. While the Type-I heterostructure produces a two dimensional electron gas, the Type-II heterostructure hosts an oxygen-rich two dimensional hole gas at the interface. Furthermore, in the presence of intrinsic spin-orbit coupling, we have found evidence of both cubic and linear Rashba interactions in the conduction bands of the Type-I heterostructure. On the contrary, there is spin-splitting of both the valence and the conduction bands in the Type-II interface, which are found to be only linear Rashba type. Interestingly, the Type-II interface also harbours a potential photocurrent transition path, making it an excellent platform to study the circularly polarized photogalvanic effect.

Keywords: non-magnetic heterostructure, spin-orbitronics, Rashba, photogalvanic effect

1. INTRODUCTION

Spin based electronics has taken the lead in the fast expanding field of quantum technologies for carrying information by spin instead of charge [1]. These energy-efficient devices necessarily require manipulation of local spins for efficient processing of quantum information. In recent years, manipulation of the spin degree of freedom in solid-state materials via spin-orbit coupling, especially the Rashba spin-orbit coupling, has emerged as one of the most promising approach for developing such next generation energy-efficient electronic devices [2, 3]. Dresselhaus and Rashba were the first to observe that the

* bh.sanchari@gmail.com

† dattas@nitrkl.ac.in

combined effect of the intrinsic spin-orbit coupling (SOC) and the bulk inversion asymmetry could lead to spin-split energy bands in non-centrosymmetric zinc-blende or wurtzite semiconductors [4, 5]. Later, Bychkov and Rashba [6] discovered that spin-split energy bands can also appear in two-dimensional materials due to structural inversion asymmetry of the confining potential, which is now commonly referred as Rashba spin-orbit (RSO) interaction. The advantage of controlling the RSO interaction in a material by an external electric field holds the promise to resolve the designing issues of the spintronic devices which typically arises due to the inclusion of local magnetic field [7, 8]. The motivation of designing spin-based electronic devices without the ferromagnetic elements has given rise to the rapidly emerging field of spin-orbitronics [9, 10]. The most effective method of creating spin current inside the non-magnetic materials is by spin-charge interconversion. The electrically induced regulation of the spin dynamics through spin-orbit coupling is the most practical and desirable method of achieving this interconversion [11, 12]. The principle of spin-orbitronics was first explored in semiconductors and metals, though within some years oxide-heterostructures have emerged to be the most promising platform with a plethora of unique characteristics [13]. Complex oxide heterostructures are widely studied for their numerous fascinating properties, such as 2D superconductivity, coexistence of ferromagnetism & superconductivity, colossal magnetoresistance etc. [14–17], and their promising applications in the manufacturing of next generation all-oxide solid state devices [18, 19]. The interface of a heterostructure made of complex oxide perovskites breaks the structural inversion symmetry and therefore the electron/hole gas confined at the interface experiences a potential gradient perpendicular to the conduction plane [20]. Oxide interfaces offer a flexible platform for creating, controlling, and detecting spin currents or spin textures. SrTiO₃ based surfaces and interfaces are first observed as the promising candidate for creating two dimensional electron gas (2DEG) with large transport properties and highly confined quantum well [21–23]. As SrTiO₃ has strongly correlated 3d-orbital, the effect of intrinsic SOC is expected to be strong in those surfaces and interfaces making the system a suitable platform for generating Rashba spin splitting [24]. The first evidence for RSO interaction in oxide surfaces indeed emerged in the 2DEG generated at the SrTiO₃ surface along the (0 0 1) direction [25]. Irrespective of various interesting SO-based properties in LaAlO₃/SrTiO₃ heterostructure, one of the main difficulty with this system is the presence of ferromagnetism at the interface, and the RSO interaction is dependent on the magneto-

resistance tuning [26].

To overcome this situation, there is an ongoing effort to create oxide heterostructure with non-magnetic interface and stronger SOC, and KTaO_3 has emerged as an exciting alternative for its novel electronic as well as spintronic properties due to the presence of the 5d-orbital and high Z-value. [16, 27, 28]. The carrier dependence of spin precession length is shorter in KTaO_3 than that in SrTiO_3 [25]. Due to the polar nature of KTaO_3 , the surface with TaO_2^+ or KO^- termination gives rise to naturally induced 2DEG and its counterpart two-dimensional hole gas (2DHG) at the interfaces [29, 30]. KTaO_3 , being a polar material, has wide range of properties to be used as a substrate material for its novel surface properties [31, 32]. The in-built electric field at the surface of KTaO_3 , provides an ideal system for studying RSO [33] and recently experimental evidences of spin splitting have been found in the surface bands [34, 35]. In comparison to $\text{LaAlO}_3/\text{SrTiO}_3$ heterostructure, $\text{LaAlO}_3/\text{KTaO}_3$ has larger charge carrier density at interface with high electron mobility as LaAlO_3 is also a polar material [36]. Besides, in the bulk state, KTaO_3 and LaAlO_3 are cubic with space group $\text{Pm}\bar{3}\text{m}$ (No.221). Due to the comparable band gaps and lattice parameters, LaAlO_3 and KTaO_3 are considered as very good candidates for creating heterostructure with an effective charge accumulation at the interfaces. Recently, there have been theoretical and experimental studies of $\text{LaAlO}_3/\text{KTaO}_3$ heterostructures [37, 38]. However, detailed first-principle study on the effect of intrinsic SOC and the possibility of RSO interaction has remained unexplored.

Motivated by this, in this article, we have investigated the electronic and spintronics properties of the $\text{LaAlO}_3/\text{KTaO}_3$ heterostructure for two possible interfaces, which are $\text{TaO}_2^+/\text{LaO}^+$ (Type-I) and $\text{KO}^-/\text{AlO}_2^-$ (Type-II) using density functional theory (DFT) based first-principle calculations. We have found 2DEG in Type-I heterostructure whereas Type-II system exhibit 2DHG in its interface. In the presence of SOC, Type-I system produce both the cubic and linear RSO splitting which has been originated from conduction bands. On the contrary, Type-II heterostructure predominantly produce large k-linear RSO coupling strength which has been produced from both the conduction bands and valence bands. As earlier reported in Ref. [39], the production of circularly polarized photocurrent is possible in KTaO_3 slab system where giant RSO interaction is present. Following this, we have found a possible photocurrent transition route for the Type-II system.

In the present report, first we have discussed structural and computational details in

section 2. In Section 3 we have discussed on the effective Hamiltonian for the C_{4v} little point group. Following this we have systematically reported the Type-I and Type-II system results in Section 4. The orbital contribution in the absence of SOC has been discussed in subsections 4.1 and 4.3. The explanation of RSO and spin texture for both type systems is covered in sections. 4.2 and 4.4. In section 5, we finally come to a conclusion.

2. STRUCTURAL AND COMPUTATIONAL DETAILS

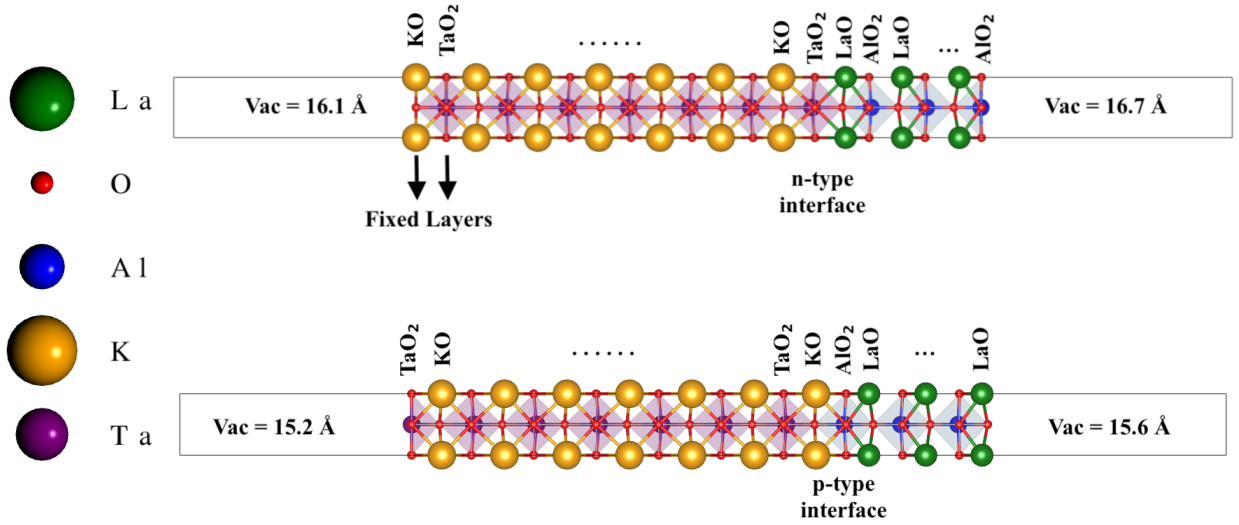


FIG. 1. The slab model for the $(\text{KTO})_{6.5}/(\text{LAO})_{2.5}$ heterostructure with $(\text{TaO}_2^+/\text{LaO}^+)$ and $(\text{KO}^-/\text{AlO}_2^-)$ interface.

In Fig. 1, we present the asymmetric slab model along $(0\ 0\ 1)$ made of $(\text{KTO})_{6.5}$ and $(\text{LAO})_{2.5}$ with two types of defect-less interfaces. No strain has been applied in the system. The perovskite oxide material with parent formula ABO_3 can be stacked as BO_2 and AO . KTaO_3 substrate comprises of alternative KO^- and TaO_2^+ layer, whereas LaAlO_3 epitaxial layers are made of LaO^+ and AlO_2^- sub-layers. To maintain the interface stoichiometry there are two possible kind of interfaces in the heterostructure created by LaAlO_3 and KTaO_3 along $(0\ 0\ 1)$ direction, i.e., $\text{TaO}_2^+/\text{LaO}^+$ and $\text{KO}^-/\text{AlO}_2^-$. Due to the asymmetry present in the heterostructures, both the systems correspond to $P4mm$ (No. 99) space group, which does not have spatial inversion symmetry or the mirror symmetry.

The first-principle density functional calculations are performed by Quantum *Espresso* (QE) package [40]. The exchange-correlation of the electron interactions are taken into

account by Perdew-Burke-Ernzerhof (PBE) functional [41]. The projector augmented wave (PAW) basis set has been used to include the interaction between valence electrons and core ions [42]. The on site Coulomb interactions of Ta-5d orbitals are considered by using the standard PBE+U method [43]. The effective value $U_{\text{eff}} = 3$ eV is employed for Ta-5d states in this work, as it is well established that such a value is appropriate to describe the strongly-correlated states of KTO [44]. Using the linear response theory implemented in the QE package we have independently verified the U value of the Ta-5d states for our heterostructures. The plane-wave basis with a cut-off energy of 75 Ry is used to expand the electronic wavefunctions. Full geometry optimizations are performed using the quick-min Verlet damped dynamics algorithm [45]. Here, Γ -centered k-point grids for sampling [46] the first Brillouin zone are set to $8 \times 8 \times 1$ for $1 \times 1 \times (m + n)$ slab models of LAO/KTO heterostructures where m and n are the number of sublayers of KTaO_3 and LaAlO_3 . Scalar relativistic effect has been taken for optimization of the structure and later on fully relativistic effect has been included in selected pseudopotentials to study the SOC effect. It has been tested that there is no significant effect of SOC in the structure optimization. As shown in Fig. 1, in the Type-I heterostructure the bottom two atomic sublayers KO and TaO_2 are kept fixed during structural optimization, while in the case of the Type-II heterostructure no layer has been kept fixed. To minimize the interaction between neighboring slabs, a vacuum layer with a thickness of ≥ 30 Å is applied along the z direction (out of plane). All atoms except those in the fixed sublayer/s are fully relaxed until the force acting on each atom is $< 10^{-3}$ Ry/Bohr. The convergence criteria of the total energy is set to be $< 10^{-4}$ Ry/Bohr. Spin-polarized calculations has been done on the slab system to check the collinear magnetism, which has been found to be zero, and hence all the SOC calculations have been conducted in the slab system by setting the initial magnetism on Ta as $0 \mu_B$. The experimental lattice parameters of bulk LaAlO_3 and KTaO_3 are 3.790 Å and 3.989 Å [47], whereas by using PBE type pseudopotential we have found the theoretical lattice parameters of KTO and LAO to be 4.02 Å and 3.81 Å, which has also been reported earlier [30]. For the heterostructures, we use an average lattice constant of 4.02 Å for both the KTO and LAO regions. The theoretical band gaps of LAO and KTO with PBE pseudopotential are 3.61 eV and 2.84 eV which are comparable with the experimental band gaps 5.6 eV and 3.5 eV respectively [48]. Unlike $\text{LaAlO}_3/\text{SrTiO}_3$ heterostructure, there is no critical thickness of epitaxial layers for insulator-to-metal transition in $\text{LaAlO}_3/\text{KTaO}_3$

heterostructure [30].

3. EFFECTIVE $\mathbf{k}\cdot\mathbf{p}$ HAMILTONIAN

The Rashba effect is a momentum-dependent spin-splitting of an energy band resulting from the combined effect of intrinsic spin-orbit interaction and broken inversion symmetry. Both the heterostructures considered in this work have c_{4v} point group symmetry. The little group has three high symmetry points when it is considered for 2D materials, which are Γ (0,0,0), X (0.5,0,0), M(0.5,0.5,0). In these systems, the splitted bands can be described by an effective two band Hamiltonian [49] at Γ point given by,

$$\begin{aligned} H_{c_{4v}} = & \alpha(k_x^2 + k_y^2) + \beta k_z^2 + \alpha_{R1}(k_x\sigma_y - k_y\sigma_x) \\ & + \alpha_{R2}k_xk_y(k_y\sigma_y - k_x\sigma_x) + \alpha_{R3}(k_x^3\sigma_y - k_y^3\sigma_x), \end{aligned} \quad (1)$$

where $\alpha_{R1}(k_x\sigma_y - k_y\sigma_x)$ is the linear RSO interaction term, whereas α_{R2} and α_{R3} are the coefficient of cubic RSO interaction. To estimate the strengths of the linear and cubic RSO interactions in our systems, we consider the $\Gamma - X$ high symmetry path. Imposing this condition we solve Eq. 1 to obtain the following two eigenvalue equations given by,

$$\epsilon_1 = \alpha k_x^2 + \alpha_{R1}k_x + \alpha_{R3}k_x^3$$

$$\epsilon_2 = \alpha k_x^2 - \alpha_{R1}k_x - \alpha_{R3}k_x^3.$$

The amount of momentum dependent spin-splitting Δ_R is given by,

$$\Delta_R = \epsilon_1 - \epsilon_2 = 2\alpha_{R1}k_x + 2\alpha_{R3}k_x^3 \quad (2)$$

The linear and cubic coupling strengths are obtained by fitting Eq. C1 to the DFT data.

4. RESULTS

In this section we discuss the aforementioned two types of interface made of LaAlO_3 and KTaO_3 . First we present the results of $\text{TaO}_2^+/\text{LaO}^+$ (type-I) interface which will be followed by $\text{KO}^-/\text{AlO}_2^-$ (type-II). The role of SOC and the origin of Rashba interactions are presented along with each of the interface.

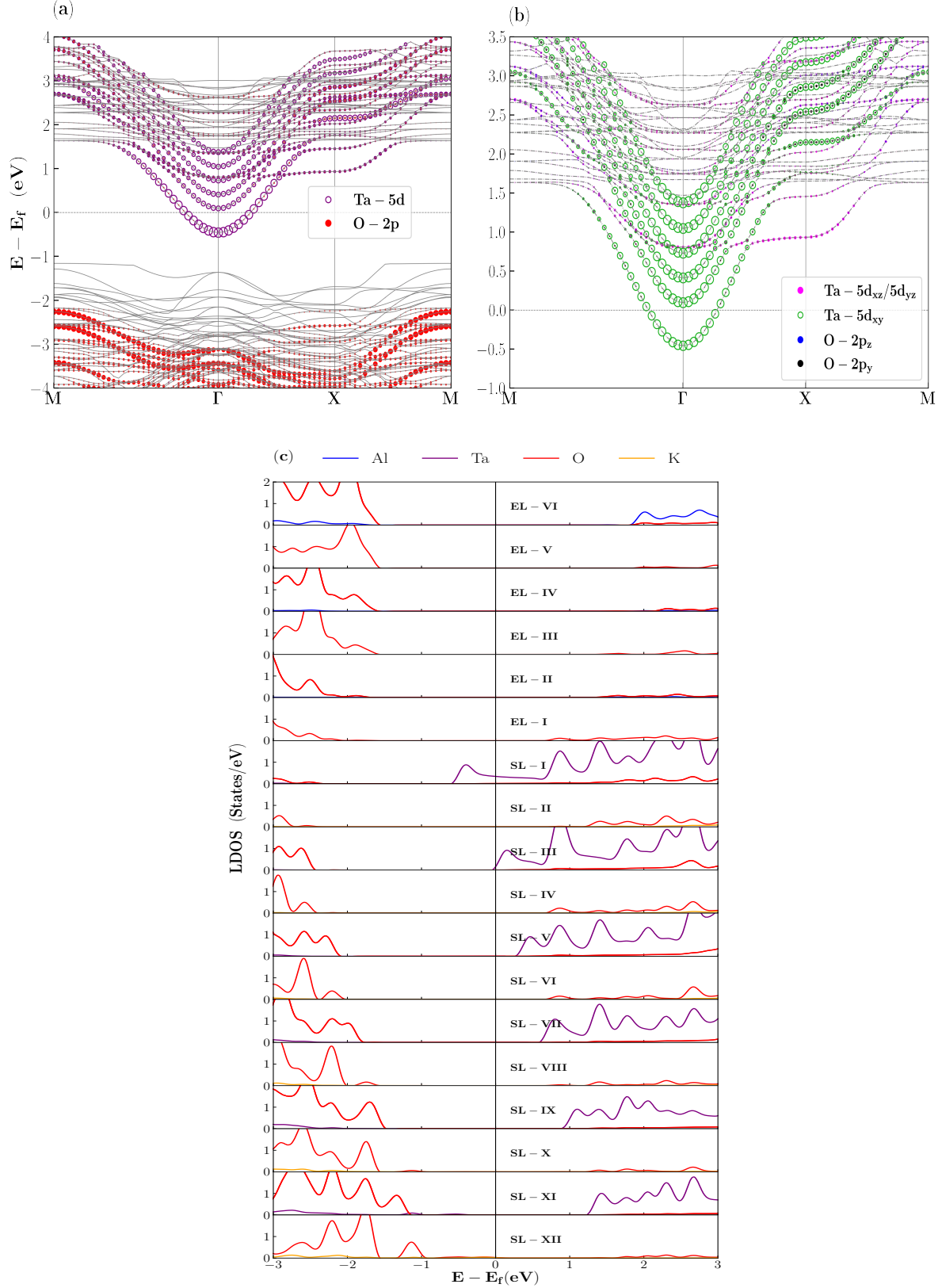


FIG. 2. (a) Band structure of the Type-I heterostructure. Grey bands represent the states originating from fixed substrate layers, (b) Zoomed-in display of the subbands coming from Ta-5d orbitals, and (c) Layer-resolved density of states for the slab system. Fixed substrate layers are not shown in the picture.

4.1. Type-I heterostructure without SOC

The $\text{TaO}_2^+/\text{LaO}^+$ interface is made by two polar end of parent materials which helps the accumulation of electron-like carriers at the interface, thereby giving rise to a 2DEG. Fig. 2(a) presents the band structure in the absence of SOC along $M-\Gamma-X-M$ high symmetry path. The band structure clearly shows that close to the Fermi energy the atomic contributions are mainly due to the Ta-5d orbitals. However, above the Fermi energy at about 1 eV or more, O-2p orbitals also contribute, albeit tiny, towards the conduction bands. However O-2p orbitals contribute significantly to form the valence bands. The zoomed-in view of the orbital contributions has been presented in Fig. 2(b).

Due to the crystal field splitting (CFS) the degeneracy of the t_{2g} orbitals of Ta-5d are lifted into a d_{xy} singlet and a d_{yz}/d_{xz} doublet. At the interface the d_{xy} band is lower in energy than the d_{yz} or d_{xz} band with a parabolic structure centered around the Γ point. Each d_{xy} band originates from individual sublayer (marked by open green circle in Fig. 2(b)), whereas all the sublayers contribute to form each of the d_{yz}/d_{xz} bands (marked by solid magenta circle in Fig. 2(b)). O-2p_y orbital hybridizes with the d_{yz}/d_{xz} orbitals. The angular momentum of d_{yz} and d_{xz} are same with opposite orientation hence the occupation of d_{yz} and d_{xz} orbitals are equal in weightage. The layer-resolved density of states (LRDOS) without spin-orbit interaction are presented in Fig. 2(c), which reconfirms that the Ta-5d orbitals are predominantly present at the interface that gives rise to the 2DEG.

A visible inter orbital crossing takes place between d_{xy} and d_{yz}/d_{xz} in the $\Gamma-X$ path. The inter-orbital crossing between d_{xy} and d_{yz}/d_{xz} bands gives the usual multiorbital (M-O) effect, which has been reported earlier at the interface of $\text{SrTiO}_3/\text{LaAlO}_3$ heterostructure [24, 26, 50, 51]. However, in contrast to this earlier reported results, in the case of $\text{KTaO}_3/\text{LaAlO}_3$ heterostructure the M-O effect is not confined within the d-orbitals. Due to the CFS, O-2p_y orbital also takes part along with the d orbitals in this kind of M-O effect. We have found that the p_y orbital hybridizes with the degenerate d_{yz}/d_{xz} orbitals, which has not been reported earlier for KTaO_3 -based 2DEG.

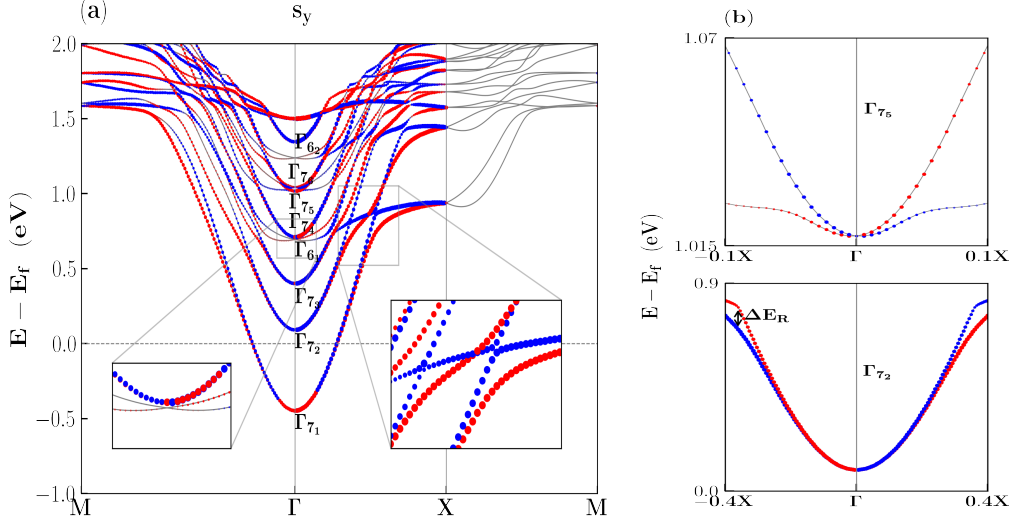


FIG. 3. (a) Spin-orbit coupling (SOC) included Ta-5d band structure with the projection of electron spins along the M- Γ -X-M direction, where non-degenerate components of Ta- t_{2g} bands are indicated by Γ_7 and Γ_6 . Red and blue colored circles represent positive and negative spin polarization along y direction. The circle size represent the weight of the spin. M-O crossing is shown in the inset of (a). (b) Rashba spin splitting are shown for the Γ_{7_2} and Γ_{7_5} bands. ΔE_R represents the maximum splitting. The direction of spin projections are perpendicular to x -direction.

4.2. Type-I heterostructure with SOC

Fig. 3(a) shows the band structure along M – Γ – X – M of the Type-I interface of LAO/KTO heterostructure in the presence of SOC. The spin polarizations are shown (solid red and blue circles) for the s_y component of the spin angular momentum. In Appendix A, the spin polarization of s_x and s_z states are shown in Fig. 8(a) and (b). The spin-split Ta-5d orbitals are presented in the left panel. According to the earlier report, the amount of RSO splitting is dependent on the M-O effect present in the system [24, 26, 50, 51]. In Ref. [26], it is found that larger the M-O effect smaller is the RSO splitting. To study the RSO effect, we have confined our study only along the Γ – X path. In the presence of SOC, all the Ta-5d bands break into the Γ_7 and Γ_6 levels. Γ_7 levels have orbital character of d_{xy} . In Fig. 3(a), we have presented all the Γ_7 levels and two Γ_6 levels. Γ_{7_1} level originates from the d_{xy} subband of substrate layer (SL-I), and it has no spin-splitting. Systematic study of every Γ_7 level reveals that the spin-splitting gets stronger as we move away from the interface. Γ_{7_2} level has almost no splitting near $k=0$, whereas for larger k value (around 0.28 \AA^{-1}) it has a

TABLE I. The table represents the RSO coupling strength obtained by fitting Eqn. C1 with calculated DFT band dispersion data along $\Gamma - X$. Corresponding plots are shown in supplemental material.

Orbital (Band Level)	α_{R1} (eVÅ)	α_{R3} (eVÅ ³)
$d_{xy}(\Gamma_{7_1})$	–	–
$d_{xy}(\Gamma_{7_2})$	0.8×10^{-3}	0.80
$d_{xy}(\Gamma_{7_3})$	2.4×10^{-3}	0.98
$d_{xy}(\Gamma_{7_4})$	–	–
$d_{xy}(\Gamma_{7_5})$	0.04	39.14
$d_{xy}(\Gamma_{7_6})$	0.26	113.42

splitting at the band crossing region, and it is predominantly cubic like with a RSO coupling strength $\alpha_{R3} = 80 \text{ eVÅ}^3$. Γ_{7_3} has a similar nature like Γ_{7_2} level. The RSO interaction is cubic like with $\alpha_{R3} = 0.98 \text{ eVÅ}^3$ at $k_x \approx 0.13 \text{ Å}$. In the Γ_{7_5} and Γ_{7_6} levels, for $k_x \lesssim 0.02 \text{ Å}$ the linear RSO interaction strength is one order magnitude higher than the cubic type RSO with $\alpha_{R1} = 43 \text{ meVÅ}$ and $\alpha_{R1} = 260 \text{ meVÅ}$. It is worthy to mention that in a recent study on $TaAs_2$ semimetal, the maximum spin splitting in Ta has been found to be 269 meV [52]. In this article we have found that a larger splitting in Ta can be achieved by using oxide heterostructure of Ta-based material. Γ_{7_4} level shows a spin flipping across the $\Gamma - X$ path (shown in the left inset of Fig. 3(a)). However, there is no spin-splitting of the bands, and it shows similar behavior to the Γ_{7_1} level. The Γ_6 level, which is a complicated combination of d_{yz}/d_{xz} and O-2p_y subbands, shows a spin-splitting. However, this spin-splitting is not Rashba-like. We have estimated the RSO coupling strengths of each spin-splitting levels by fitting Eq. C1 to our DFT data, and the results are presented in Table III. To study the nature of the spin-splitting we have plotted spin texture of the corresponding bands in the $k_x - k_y$ plane at a particular energy-cut (light green arrows present the inner band spin orientations and brown arrows present the outer band spin orientations.) Fig. 4(a) shows the spin texture of Γ_{7_2} band at iso-energy $E = E_f + 0.19 \text{ eV}$. It is evident that at lower energy, around $k=0$, there is no spin-splitting of Γ_{7_2} band. However, as pointed out earlier, at about $E = E_f + 0.69 \text{ eV}$, there is a lateral shift of up and down spin for inner and outer energy

bands (figure not shown). Fig. 4(b) shows the spin texture of Γ_{7_5} level at $E = E_f + 1.019$ eV. This spin texture reconfirms the linear RSO interaction in these bands up-to $k_x \approx 0.02 \text{ \AA}$.

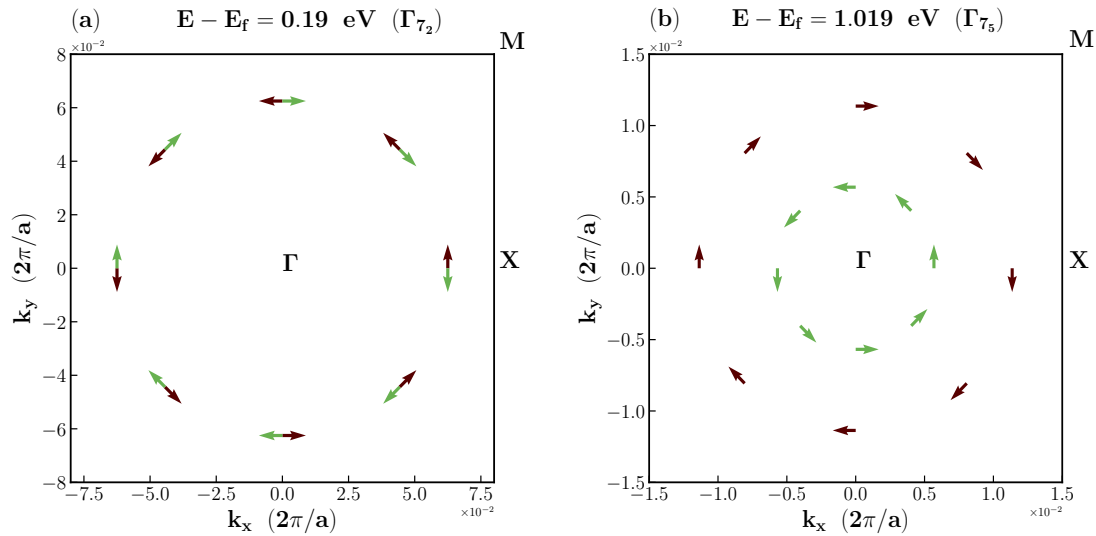


FIG. 4. (a) Associated spin-texture of Γ_{7_2} band in the 2D first Brillouin zone at iso-energy $E - E_f = 0.19$ eV, (b) Spin-texture of Γ_{7_5} at iso-energy $E - E_f = 1.019$ eV. Brown and green colors distinguish between the two splitted bands with opposite spin orientation. The length of the arrows are in unit of \hbar .

4.3. Type-II heterostructure without SOC

Fig. 5(a) presents the band structure for Type-II system without SOC along $M-\Gamma-X-M$ high symmetry path. O-2p orbitals (marked with solid red circles) are originated from the polar interface created by KO^- and AlO_2^- . Band structure shows that the conduction bands are consisted of Ta-5d subbands (marked by open purple circle) which arise from the $KTaO_3$ substrate. The parabolic nature of conduction bands around Γ indicates that there is a creation of quantum well. All the epitaxial and substrate layers are allowed to be relaxed in this heterostructure. Coexistence of electron and hole gas have been observed at Γ and X point respectively, in contrast to the earlier reported result [53] for $KTaO_3$ thin film, where similar coexistence is reported at Γ and M respectively. Furthermore, we have found that this qualitative feature remains unaltered in the case when the last substrate layer is kept fixed. These results have been presented in the supplemental information. In Fig. 5(b) we have presented the individual orbital contributions of Ta-5d and O-2p orbitals

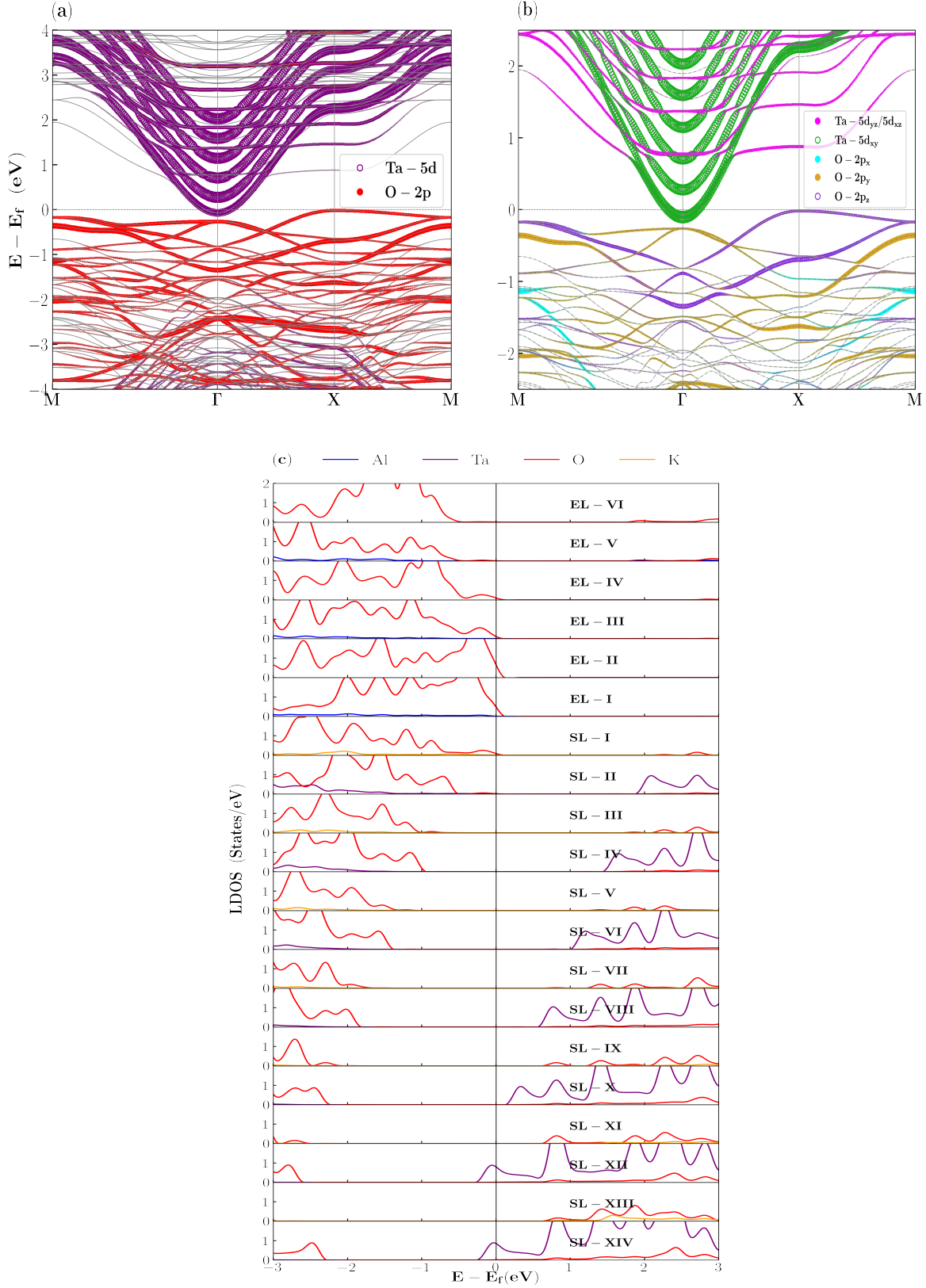


FIG. 5. (a) Band structure of the Type-II heterostructure without SOC. (b) Zoomed-in display of the subbands coming from Ta-5d and O-2p orbitals, and (c) Layer-resolved density of states for the slab system.

in the system. It is evident that similar to the Type-I heterostructure, the the degeneracy of the t_{2g} subband of Ta-5d orbital is lifted in an identical manner. Moreover, there is a similar inter-orbital crossing of d_{xy} and d_{yz}/d_{xz} bands in this Type-II hetero-interface. In this oxygen-rich interface CFS also plays a crucial role in O-2p orbital splitting. After orbital separation, the valence bands become an admixture of $p_y + p_x$ orbitals originated from SL-I and $p_y + p_z$ orbitals, originated from EL-I and EL-II. LRDOS for KO^-/AlO_2^- heterostructure reconfirms the formation of O-rich interface, which presented in Fig. 5(c). Since both the substrate and the epitaxial layers at the interface are made of negatively charged surfaces, the occurrence of hole gas is expected. This can be seen from the valence band maxima (VBM) at X (0.5,0,0) (Fig. 10 shown in Appendix B) which is primarily composed of O- $p_y + p_z$ orbitals. The carrier density in this interface is found to be $3.35 \times 10^{14} \text{ cm}^{-2}$.

4.4. Type-II heterostructure with SOC

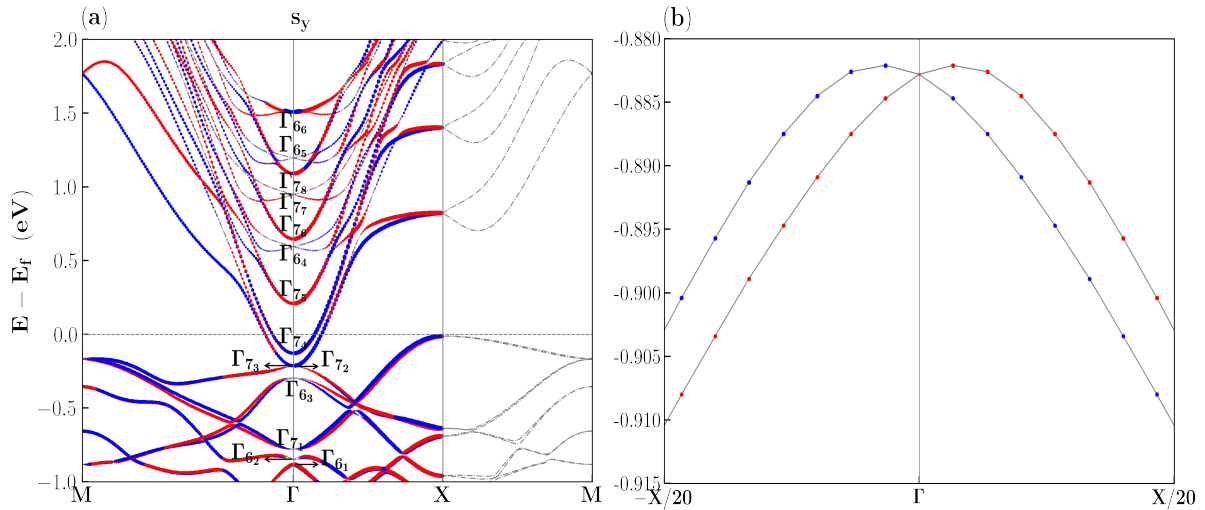


FIG. 6. (a) SOC included band structure along $M - \Gamma - X - M$ contributed by Ta-5d and O-2p orbitals. Red and blue colored circles represent up and down spin polarization along s_y . The circle size represent the weight of the spin. (b) Rashba spin-split band of Γ_{61} level.

In this subsection, we have studied Type-II heterostructure in the presence of SOC, and the corresponding band structure is presented in the Fig. 6. The presence of SOC in Type-II system leads to the formation of the Γ_6 and Γ_7 levels. Distinct Γ_6 and Γ_7 levels are

TABLE II. The table represents the RSO coupling strength for Type-II system obtained by fitting Eqn. C1 with calculated DFT band dispersion data. Corresponding plots are shown in supplemental material.

Orbital (Band Level)	α_{R1} (eVÅ)	α_{R3} (eVÅ ³)
O-2p _y + 2p _z (Γ_{61})	0.25	-182.21
Ta-5d _{xy} (Γ_{73})	1.41×10^{-2}	-2.26
Ta-5d _{xy} (Γ_{74})	2.88×10^{-2}	-1.17×10^{-2}
Ta-5d _{xy} (Γ_{75})	2.35×10^{-3}	0.59
Ta-5d _{xy} (Γ_{76})	4.30×10^{-3}	4.60×10^{-2}
Ta-5d _{yz} /d _{zx} (Γ_{66})	0.11	-94.60

indicated in the band structure by the numerals 1, 2, 3 etc. Unlike Type-I system, here both the Γ_6 and Γ_7 levels show RSO spin splitting. This is an oxygen-rich heterojunction, and in contrast to the Type-I heterostructure, in this system O-2p orbitals exhibit RSO-splitting in the valence band region. Γ_{61} band is a hybridized state of O-2p_y + p_z. In the valence band region, only Γ_{61} band shows Rashba-like spin splitting with $\alpha_{R1} \approx 250$ meVÅ and $\alpha_{R3} \approx 182.2$ eVÅ³. Surprisingly, we have observed almost a three-fold increase in α_{R1} and more than ten-fold decrease in α_{R3} values when the final substrate layer is kept fixed. These results have been presented in the supplemental information. The spin-split Γ_{61} band has been presented in Fig. 6(b). Γ_{73} , Γ_{74} , Γ_{75} , Γ_{76} are originated from Ta-5d_{xy} levels of different substrate layers. The RSO spin splitting of these levels are predominantly cubic in nature. In Γ_{62} , Γ_{63} , Γ_{64} , Γ_{65} and Γ_{71} , Γ_{72} , Γ_{77} , Γ_{78} (which are not shown in Table IV) there is a continuous flipping between the two spin channels in the immediate neighbourhood of the Γ point, and hence the observed spin-splitting in these levels are not categorized as RSO spin splitting. Γ_{66} level is originated from Ta-5d_{yz}/d_{zx} band and it has predominantly linear RSO coupling strength of $\alpha_{R1} \approx 110$ meVÅ. The spin channel in this band survives upto $\frac{X}{20}$ away from $k = 0$. The linear and cubic Rashba coupling strengths for all the spin-split levels are presented in the Table IV.

Interestingly, the Type-II system is found to be an ideal system to explore CPGE because it is a member of the C_{4v} point group and possesses a large k-linear RSO splitting with

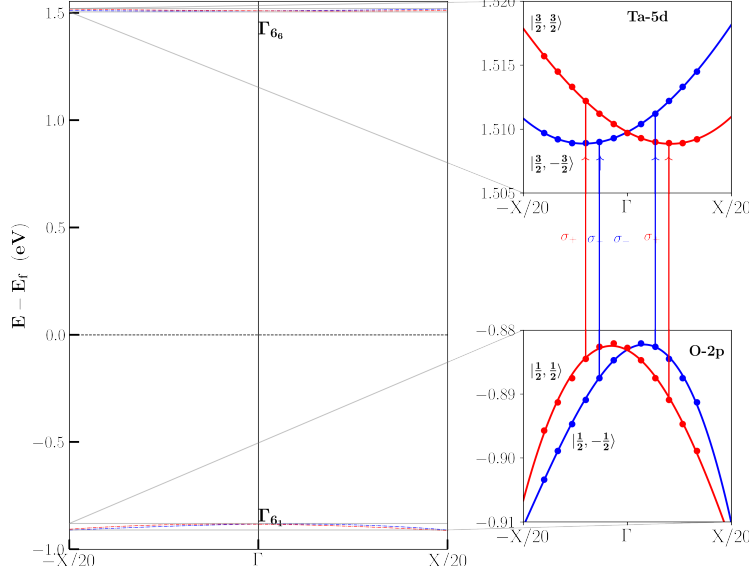


FIG. 7. Schematic representation of circularly polarized photogalvanic effect for Type-II system. σ_+ (red) and σ_- (blue) are the right handed and left handed polarized light. Red and blue arrows show the possible transitions.

electron spin polarization along k_x . Fig. 7 is a schematic representation of the possible electronic arrangement for producing circularly polarized photocurrent in the system which may provide a likely explanation for the recent experimental observation of CPGE in the LAO/KTO heterostructure [54]. In this system, the required optical transitions for CPGE take place between Γ_{6_1} and Γ_{6_6} levels. For the right-handed polarized light (σ_+), the interband transition is possible only for $|j, m_j\rangle = |\frac{1}{2}, \frac{1}{2}\rangle \rightarrow |\frac{3}{2}, \frac{3}{2}\rangle$ and similarly for left handed polarized light (σ_-) the only possible transition is $|j, m_j\rangle = |\frac{1}{2}, -\frac{1}{2}\rangle \rightarrow |\frac{3}{2}, -\frac{3}{2}\rangle$. Γ_{6_1} and Γ_{6_6} levels are originated from the O-2p and Ta-5d bands of the EL-I and SL-IV, respectively. Surprisingly, this qualitative feature remains unaltered for the same system with fixed substrate layer. However, the transition route of the photocurrent is different for the later case. The results for Type-II system with fixed substrate layer have been presented elaborately in the supplemental material.

5. CONCLUSION

In conclusion, $\text{TaO}_2^+/\text{LaO}^+$ and $\text{KO}_2^-/\text{AlO}_2^-$, both of which are referred to as Type-I and Type-II stoichiometric interfaces, has been individually explored in this work. We have

investigated the band dispersion characteristics along the $\Gamma - X$ path for both the systems without and with SOC. We have found that, Ta-5d_{xy} bands can produce the strongest k-linear RSO for Type-I systems with a strength up to 260 meVÅ, while the k³-RSO coupling can attain a value up-to 113.42 eVÅ³. In this Type-I heterostructure, no RSO splitting is observed in Ta-5d_{yz}/d_{zx} bands. However, Type-II system predominantly produce k-linear RSO in both the Ta-5d and O-2p orbitals. The maximum linear RSO coupling strength for this system is estimated to be 250 meVÅ in O-2p band and 110 meVÅ in Ta-5d band. Furthermore, we have discovered a possible optical transition path in this Type-II system that may give rise to the circular photogalvanic effect, which is still quite rare in oxide heterostructures.

6. ACKNOWLEDGEMENTS

The authors would like to thank the computational facility provided by the National Institute of Technology, Rourkela. SB would like to thank Sri Sandipan Dasgupta, Bhaba Atomic Research Centre, VECC, Kolkata, India, for very useful discussions.

-
- [1] A. Hirohata, K. Yamada, Y. Nakatani, I.-L. Prejbeanu, B. Diény, P. Pirro, and B. Hillebrands, Review on spintronics: Principles and device applications, *Journal of Magnetism and Magnetic Materials* **509**, 166711 (2020).
- [2] D. Bercioux and P. Lucignano, Quantum transport in rashba spin-orbit materials: a review, *Reports on Progress in Physics* **78**, 106001 (2015).
- [3] S. Manipatruni, D. E. Nikonov, C.-C. Lin, T. A. Gosavi, H. Liu, B. Prasad, Y.-L. Huang, E. Bonturim, R. Ramesh, and I. A. Young, Scalable energy-efficient magnetoelectric spin-orbit logic, *Nature* **565**, 35 (2019).
- [4] G. Dresselhaus, Spin-orbit coupling effects in zinc blende structures, *Physical Review* **100**, 580 (1955).
- [5] E. Rashba, Properties of semiconductors with an extremum loop. i. cyclotron and combinational resonance in a magnetic field perpendicular to the plane of the loop, *Sov. Phys.-Solid State* **2**, 1109 (1960).
- [6] Y. A. Bychkov and É. I. Rashba, Properties of a 2d electron gas with lifted spectral degeneracy, *JETP lett* **39**, 78 (1984).
- [7] D. Awschalom and N. Samarth, Spintronics without magnetism, *Physics* **2**, 50 (2009).
- [8] J. H. Dil, Spin and angle resolved photoemission on non-magnetic low-dimensional systems, *Journal of Physics: Condensed Matter* **21**, 403001 (2009).
- [9] A. Soumyanarayanan, N. Reyren, A. Fert, and C. Panagopoulos, Emergent phenomena induced by spin-orbit coupling at surfaces and interfaces, *Nature* **539**, 509 (2016).
- [10] F. Trier, P. Noël, J.-V. Kim, J.-P. Attané, L. Vila, and M. Bibes, Oxide spin-orbitronics: spin-charge interconversion and topological spin textures, *Nature Reviews Materials* **7**, 258 (2022).
- [11] D. C. Vaz, P. Noël, A. Johansson, B. Göbel, F. Y. Bruno, G. Singh, S. Mckeown-Walker, F. Trier, L. M. Vicente-Arche, A. Sander, *et al.*, Mapping spin-charge conversion to the band structure in a topological oxide two-dimensional electron gas, *Nature materials* **18**, 1187 (2019).
- [12] A. Manchon, H. C. Koo, J. Nitta, S. Frolov, and R. Duine, New perspectives for rashba spin-orbit coupling, *Nature materials* **14**, 871 (2015).

- [13] M. Bibes, J. E. Villegas, and A. Barthélémy, Ultrathin oxide films and interfaces for electronics and spintronics, *Advances in Physics* **60**, 5 (2011).
- [14] A. Brinkman, M. Huijben, M. Van Zalk, J. Huijben, U. Zeitler, J. Maan, W. G. van der Wiel, G. Rijnders, D. H. Blank, and H. Hilgenkamp, Magnetic effects at the interface between non-magnetic oxides, *Nature materials* **6**, 493 (2007).
- [15] R. Pentcheva and W. E. Pickett, Electronic phenomena at complex oxide interfaces: insights from first principles, *Journal of Physics: Condensed Matter* **22**, 043001 (2010).
- [16] H. Y. Hwang, Y. Iwasa, M. Kawasaki, B. Keimer, N. Nagaosa, and Y. Tokura, Emergent phenomena at oxide interfaces, *Nature materials* **11**, 103 (2012).
- [17] J. M. Rondinelli and N. A. Spaldin, Structure and properties of functional oxide thin films: insights from electronic-structure calculations, *Advanced materials* **23**, 3363 (2011).
- [18] Y. Ohno, D. Young, B. a. Beschoten, F. Matsukura, H. Ohno, and D. Awschalom, Electrical spin injection in a ferromagnetic semiconductor heterostructure, *Nature* **402**, 790 (1999).
- [19] L. He, J. A. S. Oh, J. J. J. Chua, and H. Zhou, Synthesis and interface modification of oxide solid-state electrolyte-based all-solid-state lithium-ion batteries: Advances and perspectives, *Functional Materials Letters* **14**, 2130002 (2021).
- [20] R. Winkler, Rashba spin splitting in two-dimensional electron and hole systems, *Phys. Rev. B* **62**, 4245 (2000).
- [21] A. Ohtomo and H. Hwang, A high-mobility electron gas at the $\text{LaAlO}_3/\text{SrTiO}_3$ heterointerface, *Nature* **427**, 423 (2004).
- [22] Z. S. Popović, S. Satpathy, and R. M. Martin, Origin of the two-dimensional electron gas carrier density at the LaAlO_3 on SrTiO_3 interface, *Phys. Rev. Lett.* **101**, 256801 (2008).
- [23] A. Santander-Syro, O. Copie, T. Kondo, F. Fortuna, S. Pailhes, R. Weht, X. Qiu, F. Bertran, A. Nicolaou, A. Taleb-Ibrahimi, *et al.*, Two-dimensional electron gas with universal subbands at the surface of SrTiO_3 , *Nature* **469**, 189 (2011).
- [24] Z. Zhong, A. Tóth, and K. Held, Theory of spin-orbit coupling at $\text{LaAlO}_3/\text{SrTiO}_3$ interfaces and SrTiO_3 surfaces, *Phys. Rev. B* **87**, 161102 (2013).
- [25] H. Nakamura, T. Koga, and T. Kimura, Experimental evidence of cubic rashba effect in an inversion-symmetric oxide, *Physical Review Letters* **108**, 206601 (2012).
- [26] W. Kong, T. Yang, J. Zhou, Y. Z. Luo, T. Zhu, J. Chen, L. Shen, Y. Jiang, Y. P. Feng, and M. Yang, Tunable rashba spin-orbit coupling and its interplay with multiorbital effect and

- magnetic ordering at oxide interfaces, *Physical Review B* **104**, 155152 (2021).
- [27] A. D. Caviglia, M. Gabay, S. Gariglio, N. Reyren, C. Cancellieri, and J.-M. Triscone, Tunable rashba spin-orbit interaction at oxide interfaces, *Phys. Rev. Lett.* **104**, 126803 (2010).
- [28] A. Gupta, H. Silotia, A. Kumari, M. Dumen, S. Goyal, R. Tomar, N. Wadehra, P. Ayyub, and S. Chakraverty, KTaO₃-the new kid on the spintronics block, *Advanced Materials* **34**, 2106481 (2022).
- [29] Y. Wang, W. Tang, J. Cheng, M. Behtash, and K. Yang, Creating two-dimensional electron gas in polar/polar perovskite oxide heterostructures: first-principles characterization of LaAlO₃/A⁺B⁵⁺O₃, *ACS applied materials & interfaces* **8**, 13659 (2016).
- [30] Y. Wang, Z. Zhang, J. Cheng, Q. Zhang, W. Tang, and K. Yang, Creating a two-dimensional hole gas in a polar/polar LaAlO₃/KTaO₃ perovskite heterostructure, *J. Mater. Chem. C* **8**, 14230 (2020).
- [31] J. A. Li, E. Akhadov, J. Baker, L. Boatner, D. Bonart, J. Fritsch, S. Safron, U. Schröder, J. Skofronick, and T. Trelenberg, Surface structure and dynamics of KTaO₃ (001), *Physical Review B* **68**, 045402 (2003).
- [32] Z. Wang, M. Reticcioli, Z. Jakub, I. Sokolović, M. Meier, L. A. Boatner, M. Schmid, G. S. Parkinson, U. Diebold, C. Franchini, *et al.*, Surface chemistry on a polarizable surface: Coupling of co with KTaO₃ (001), *Science Advances* **8**, eabq1433 (2022).
- [33] V. Kumar and N. Ganguli, Rashba-like spin-orbit interaction and spin texture at the KTaO₃ surface from DFT calculations, *Phys. Rev. B* **106**, 125127 (2022).
- [34] P. D. C. King, R. H. He, T. Eknapakul, P. Buaphet, S.-K. Mo, Y. Kaneko, S. Harashima, Y. Hikita, M. S. Bahramy, C. Bell, Z. Hussain, Y. Tokura, Z.-X. Shen, H. Y. Hwang, F. Baumberger, and W. Meevasana, Subband structure of a two-dimensional electron gas formed at the polar surface of the strong spin-orbit perovskite ktao₃, *Phys. Rev. Lett.* **108**, 117602 (2012).
- [35] A. F. Santander-Syro, C. Bareille, F. Fortuna, O. Copie, M. Gabay, F. Bertran, A. Taleb-Ibrahimi, P. Le Fèvre, G. Herranz, N. Reyren, M. Bibes, A. Barthélémy, P. Lecoeur, J. Guevara, and M. J. Rozenberg, Orbital symmetry reconstruction and strong mass renormalization in the two-dimensional electron gas at the surface of KTaO₃, *Phys. Rev. B* **86**, 121107 (2012).
- [36] H. Zhang, H. Zhang, X. Yan, X. Zhang, Q. Zhang, J. Zhang, F. Han, L. Gu, B. Liu, Y. Chen, *et al.*, Highly mobile two-dimensional electron gases with a strong gating effect at

- the amorphous LaAlO₃/KTaO₃ interface, ACS applied materials & interfaces **9**, 36456 (2017).
- [37] M. Zapf, M. Schmitt, J. Gabel, P. Scheiderer, M. Stübinger, B. Leikert, G. Sangiovanni, L. Dudy, S. Chernov, S. Babenkov, D. Vasilyev, O. Fedchenko, K. Medjanik, Y. Matveyev, A. Gloskowski, C. Schlueter, T.-L. Lee, H.-J. Elmers, G. Schönhense, M. Sing, and R. Claessen, Hard x-ray angle-resolved photoemission from a buried high-mobility electron system, Phys. Rev. B **106**, 125137 (2022).
- [38] S. Varotto, A. Johansson, B. Göbel, L. M. Vicente-Arche, S. Mallik, J. Bréhin, R. Salazar, F. Bertran, P. L. Fèvre, N. Bergeal, *et al.*, Direct visualization of rashba-split bands and spin/orbital-charge interconversion at KTaO₃ interfaces, Nature Communications **13**, 1 (2022).
- [39] N. Wu, X.-J. Zhang, and B.-G. Liu, Strain-enhanced giant rashba spin splitting in ultrathin KTaO₃ films for spin-polarized photocurrents, RSC advances **10**, 44088 (2020).
- [40] P. Giannozzi, S. Baroni, N. Bonini, M. Calandra, R. Car, C. Cavazzoni, D. Ceresoli, G. L. Chiarotti, M. Cococcioni, I. Dabo, *et al.*, Quantum espresso: a modular and open-source software project for quantum simulations of materials, Journal of physics: Condensed matter **21**, 395502 (2009).
- [41] J. P. Perdew, K. Burke, and M. Ernzerhof, Generalized gradient approximation made simple, Phys. Rev. Lett. **77**, 3865 (1996).
- [42] P. E. Blöchl, Projector augmented-wave method, Phys. Rev. B **50**, 17953 (1994).
- [43] M. Cococcioni and S. de Gironcoli, Linear response approach to the calculation of the effective interaction parameters in the LDA + U method, Phys. Rev. B **71**, 035105 (2005).
- [44] S. Xu, F. Jia, S. Hu, A. Sundaresan, N. V. Ter-Oganessian, A. P. Pyatakov, J. Cheng, J. Zhang, S. Cao, and W. Ren, Predicting the structural, electronic and magnetic properties of few atomic-layer polar perovskite, Phys. Chem. Chem. Phys. **23**, 5578 (2021).
- [45] D. Sheppard, R. Terrell, and G. Henkelman, Optimization methods for finding minimum energy paths, The Journal of chemical physics **128**, 134106 (2008).
- [46] H. J. Monkhorst and J. D. Pack, Special points for brillouin-zone integrations, Physical review B **13**, 5188 (1976).
- [47] W.-H. Yang, D.-S. Hou, C.-Z. Li, H. Fan, and H. Y. Zhang, LaAlO₃ single crystal substrate for epitaxial superconducting thin films, Solid State Communications **75**, 421 (1990).
- [48] S. H. Wemple, Some transport properties of oxygen-deficient single-crystal potassium tantalate (KTaO₃), Phys. Rev. **137**, A1575 (1965).

- [49] S. Vajna, E. Simon, A. Szilva, K. Palotas, B. Ujfalussy, and L. Szunyogh, Higher-order contributions to the rashba-bychkov effect with application to the Bi/Ag(111) surface alloy, *Phys. Rev. B* **85**, 075404 (2012).
- [50] G. Khalsa, B. Lee, and A. H. MacDonald, Theory of t_{2g} electron-gas rashba interactions, *Phys. Rev. B* **88**, 041302(R) (2013).
- [51] P. King, S. Mckeown Walker, A. Tamai, A. De La Torre, T. Eknapakul, P. Buaphet, S.-K. Mo, W. Meevasana, M. Bahramy, and F. Baumberger, Quasiparticle dynamics and spin-orbital texture of the srTiO₃ two-dimensional electron gas, *Nature communications* **5**, 3414 (2014).
- [52] A. S. Wadge, G. Grabecki, C. Autieri, B. J. Kowalski, P. Iwanowski, G. Cuono, M. Islam, C. M. Canali, K. Dybko, A. Hruban, *et al.*, Electronic properties of TaAs₂ topological semimetal investigated by transport and arpes, *Journal of Physics: Condensed Matter* **34**, 125601 (2022).
- [53] X.-J. Zhang and B.-G. Liu, Strain-driven carrier-type switching of surface two-dimensional electron and hole gases in a KTaO₃ thin film, *Phys. Chem. Chem. Phys.* **20**, 24257 (2018).
- [54] S. Wang, H. Zhang, J. Zhang, S. Li, D. Luo, J. Wang, K. Jin, and J. Sun, Circular photogalvanic effect in oxide two-dimensional electron gases, *Phys. Rev. Lett.* **128**, 187401 (2022).

Appendix A: Spin polarized band-structures of Type-I

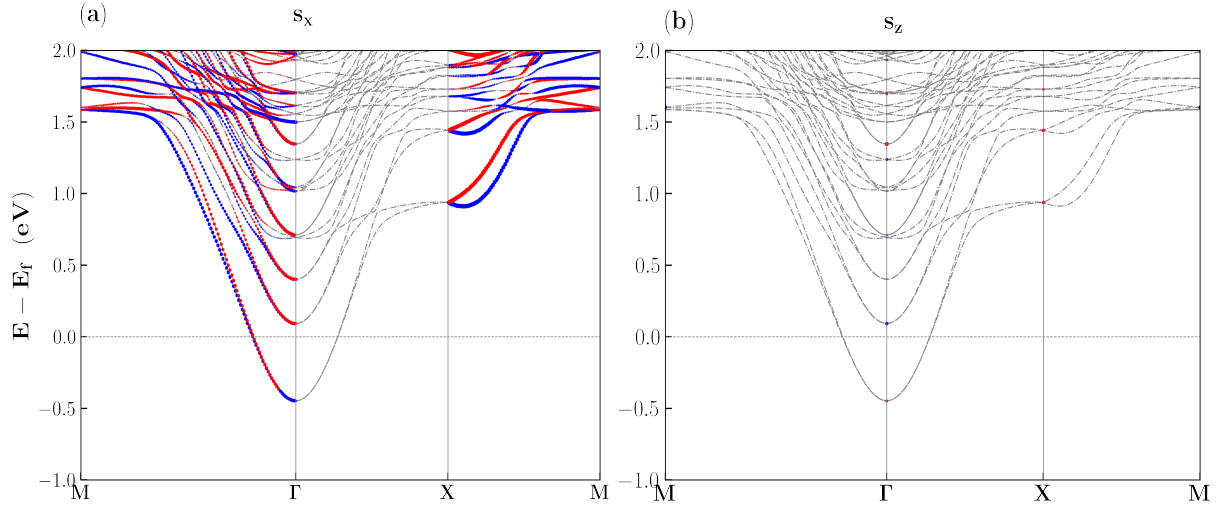


FIG. 8. (a) and (b) show SOC included band structures of the Type-I heterostructure with the projection of electron spins to s_x and s_z , respectively. Red and blue dots denote up and down components of spin projections, respectively. The size of the dot shows the relative amplitude of the corresponding spin component.

Fig. 8(a) Fig. 8(b) present the band structure of Type-I system with the spin polarization along x and z direction. Along z direction there is no spin polarization present in the band dispersion. Along s_x , there is spin polarization, although we have not studied this system in detail.

Appendix B: Spin polarized band-structures of Type-II

Fig. 9(a) Fig. 9(b) show the Type-II system's band structure with spin polarization in the x and z directions. The band dispersion exhibits no spin polarization in the direction of z. Spin polarization exists along s_x , however we have not thoroughly examined this system. At the HS point X (0.5,0,0), the valence band maxima has been seen. The RSO splitting along the M-X-M HS path is cubic-like. This paper does not contain a full discussion of this observation since we have restricted our analysis to the $\Gamma - X$ path.

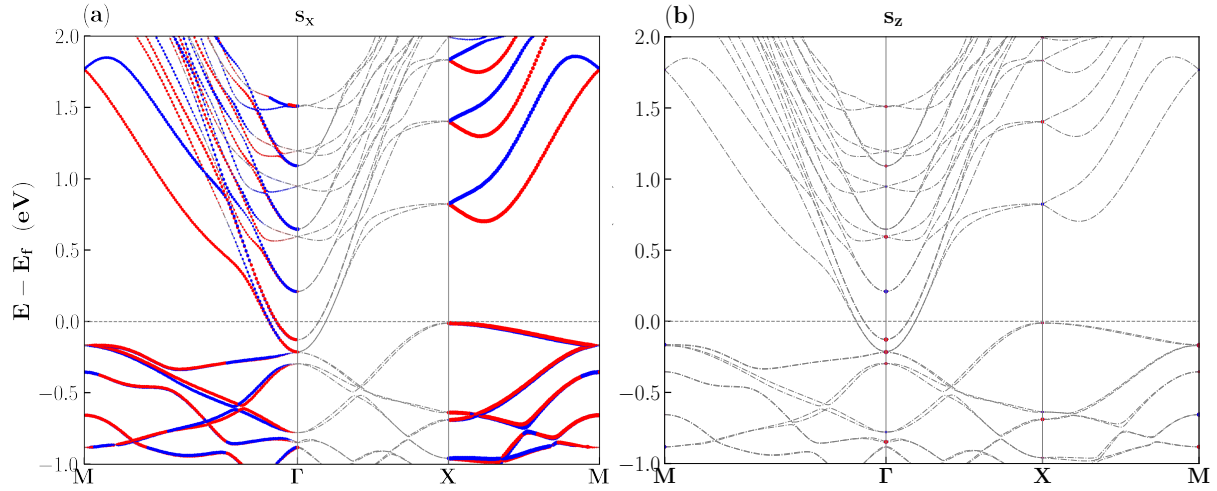


FIG. 9. (a) and (b) show SOC included band structures of the Type-II heterostructure with the projection of electron spins to s_x and s_z , respectively. Red and blue dots denote up and down components of spin projections, respectively. The size of the dot shows the relative amplitude of the corresponding spin component.

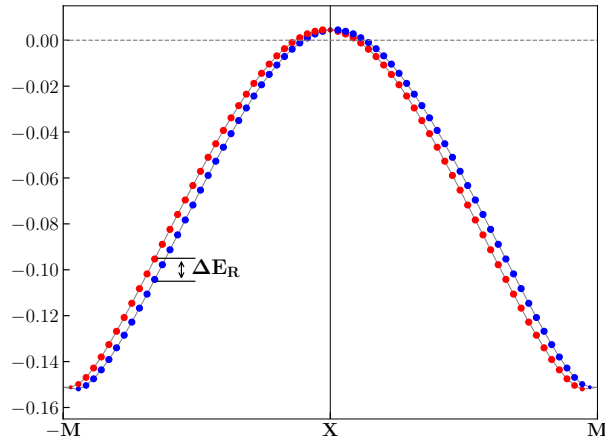


FIG. 10. (a) SOC included band structures of the Type-II heterostructure along M-X-M with the projection of electron spins s_y . It represents that the VBM of Type-II system is appeared at the X (0.5,0,0) HS point.

Appendix C: Fitting equation obtained from Hamiltonian

$$\Delta_R = \epsilon_1 - \epsilon_2 = 2\alpha_{R1}k_x + 2\alpha_{R3}k_x^3 \quad (\text{C1})$$

1. Fitting for RSO parameter in Type-I heterostructure

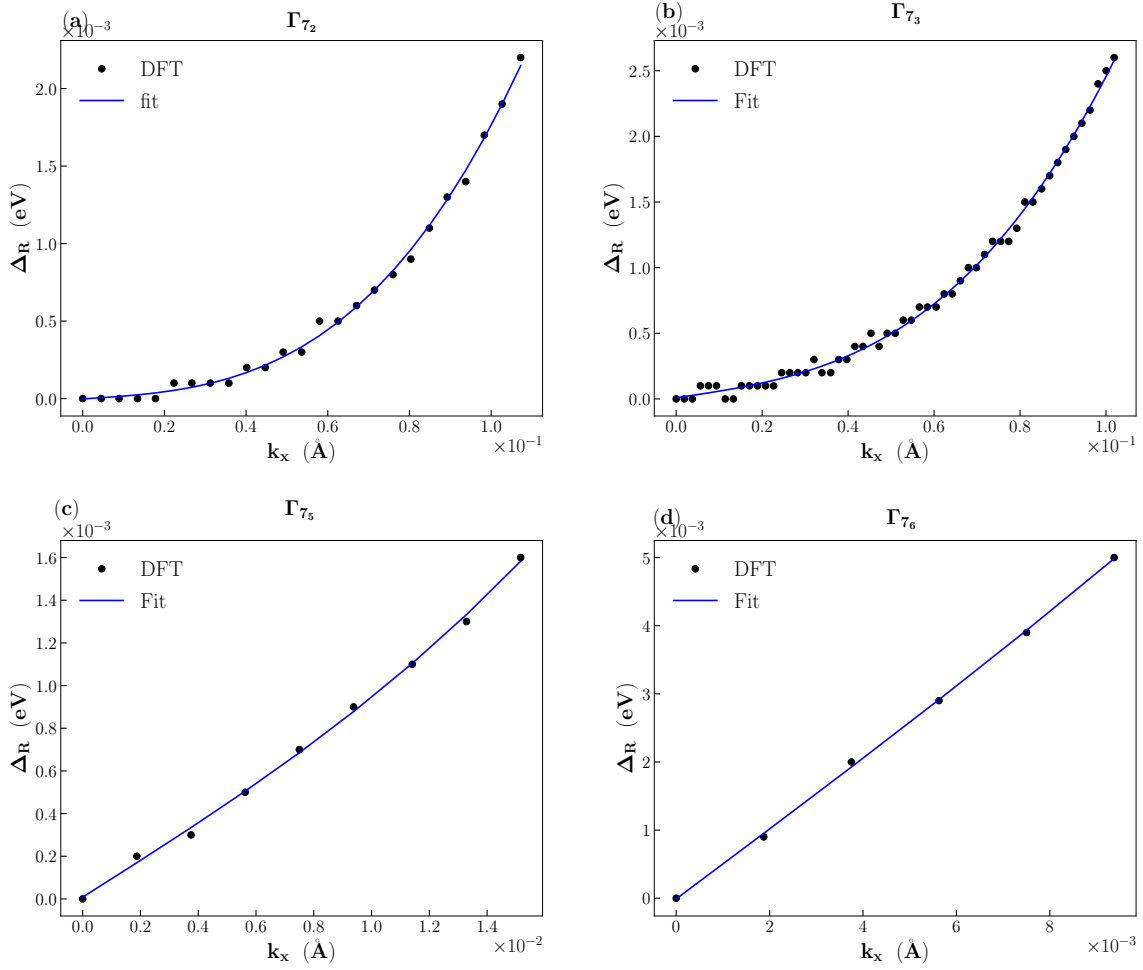


FIG. 11. Hamiltonian fitting by using eqn. C1 for (a) Γ_{7_2} (b) Γ_{7_3} (c) Γ_{7_5} (d) Γ_{7_6} bands

TABLE III. The table represents the RSO coupling strength obtained by fitting Eqn. C1 with calculated DFT band dispersion data along $\Gamma - X$. Corresponding plots are presented in Fig. 11.

Orbital (Band Level)	α_{R1} (eVÅ)	α_{R3} (eVÅ ³)
$d_{xy}(\Gamma_{7_1})$	–	–
$d_{xy}(\Gamma_{7_2})$	0.8×10^{-3}	0.80
$d_{xy}(\Gamma_{7_3})$	2.4×10^{-3}	0.98
$d_{xy}(\Gamma_{7_4})$	–	–
$d_{xy}(\Gamma_{7_5})$	0.04	39.14
$d_{xy}(\Gamma_{7_6})$	0.26	113.42

2. Fitting for RSO parameter in Type-II heterostructure without any fixed substrate layer

TABLE IV. The table represents the RSO coupling strength for Type-II system obtained by fitting Eqn. C1 with calculated DFT band dispersion data. Corresponding plots are shown Fig 12.

Orbital (Band Level)	α_{R1} (eVÅ)	α_{R3} (eVÅ ³)
O-2p _y + 2p _z (Γ_{6_1})	0.25	-182.21
Ta-5d _{xy} (Γ_{7_3})	1.41×10^{-2}	-2.26
Ta-5d _{xy} (Γ_{7_4})	2.88×10^{-2}	-1.17×10^{-2}
Ta-5d _{xy} (Γ_{7_5})	2.35×10^{-3}	0.59
Ta-5d _{xy} (Γ_{7_6})	4.30×10^{-3}	4.60×10^{-2}
Ta-5d _{yz} /d _{zx} (Γ_{6_6})	0.11	-94.60

Appendix D: Type-II heterostructure with fixed layer

In this section, we have presented the Type-II heterostructure by keeping the last substrate TaO₂ layer at its fixed position. First we have presented the results without the effect of SOC and it is followed by the results including the effect of SOC. Fig. 13(a)

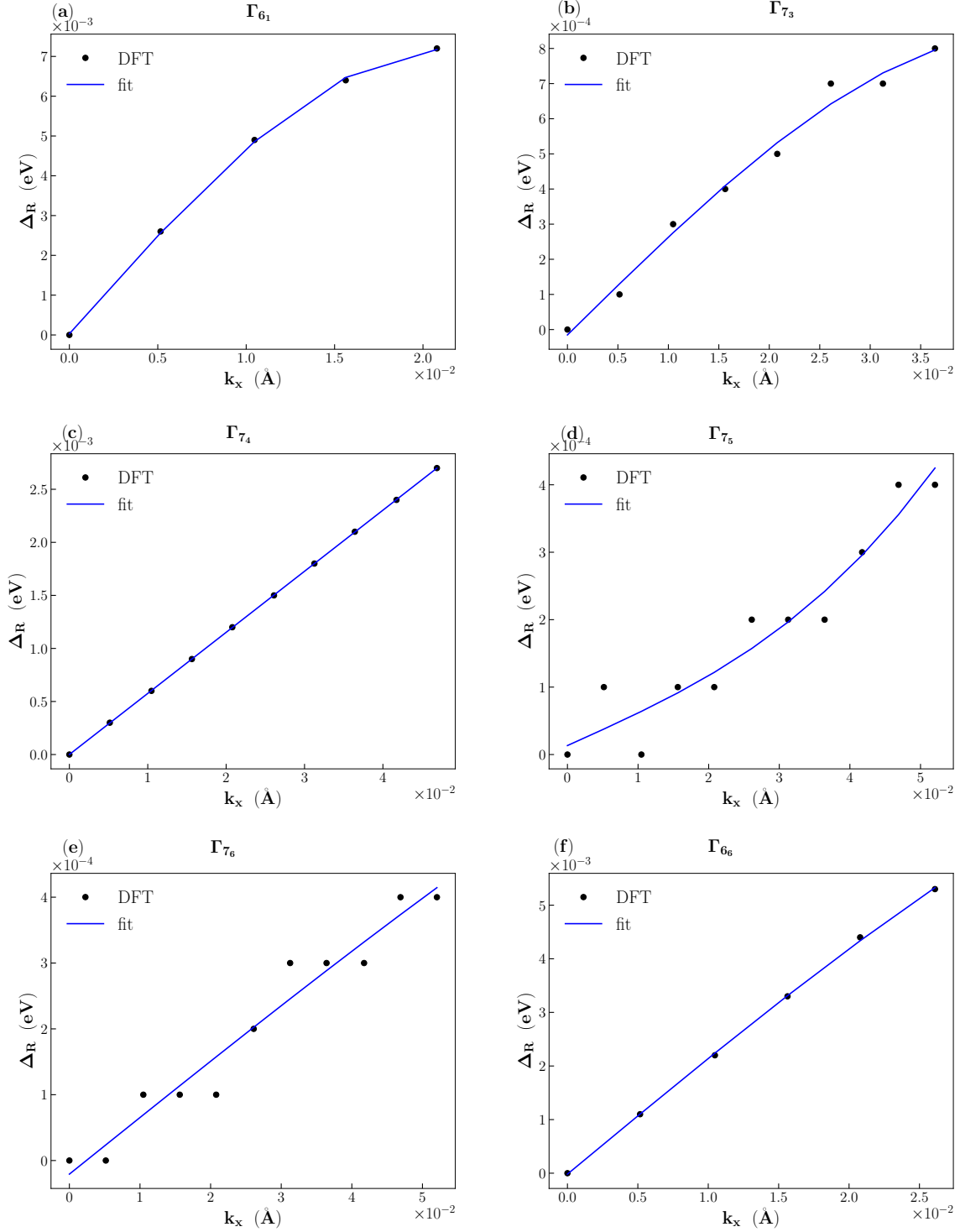


FIG. 12. Hamiltonian fitting by using eqn. C1 for (a) Γ_{61} (b) Γ_{73} (c) Γ_{74} (d) Γ_{75} (e) Γ_{76} (f) Γ_{66} bands

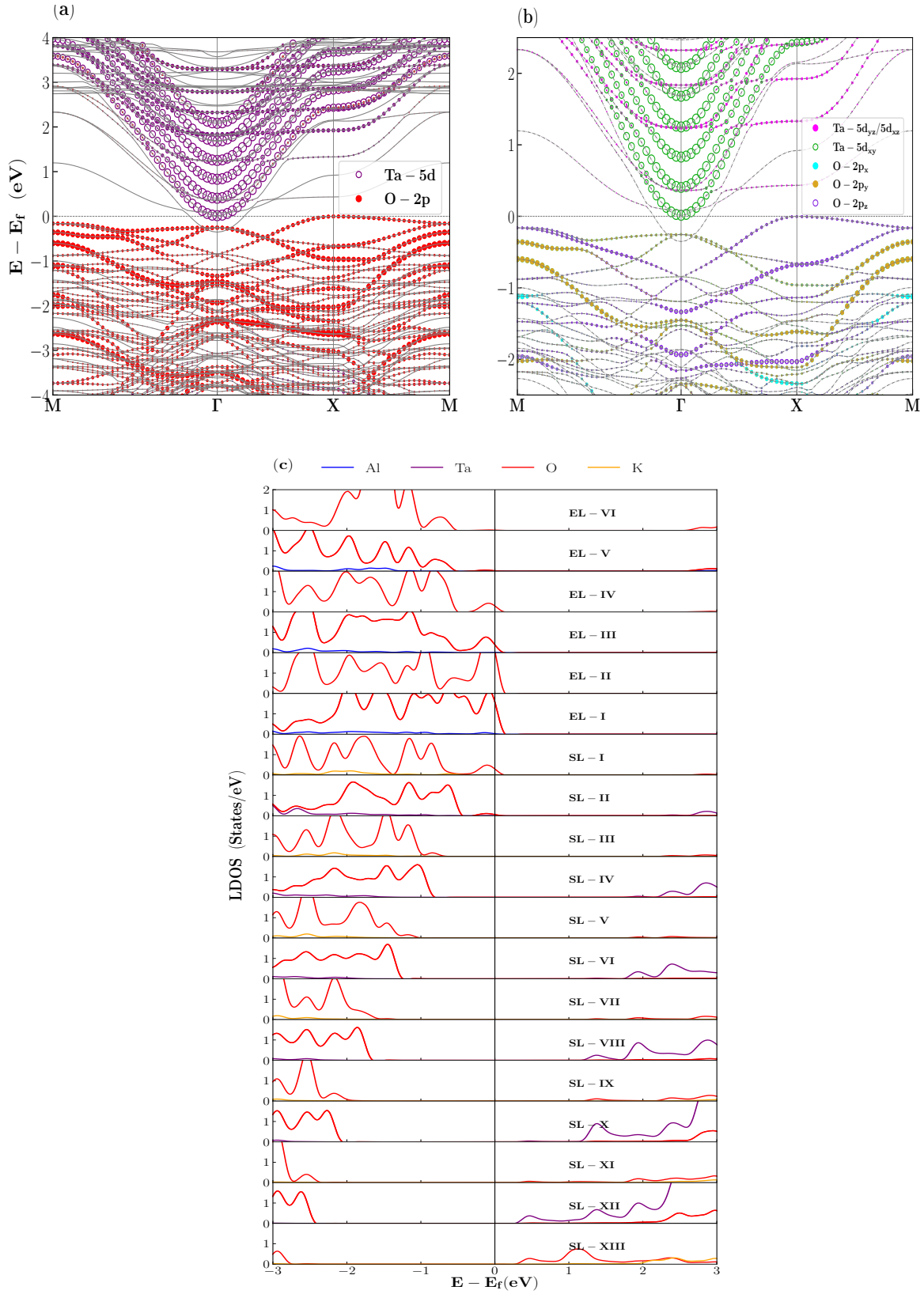


FIG. 13. (a) Band structure of the Type-II heterostructure without SOC. Grey bands represent the states originating from fixed substrate layers, (b) Zoomed-in display of the subbands coming from Ta-5d and O-2p orbitals, and (c) Layer-resolved density of states for the slab system. Fixed substrate layers are not shown in the picture.

presents the band structure for Type-II system without SOC along $M - \Gamma - X - M$ high symmetry path. O-2p orbitals (marked with solid red circles) are originated from the polar interface created by KO^- and AlO_2^- . Band structure shows that the conduction bands are consisted of Ta-5d subbands (marked by open purple circle) which arise from $KTaO_3$ substrate. The parabolic nature of conduction bands around Γ indicates that there is a creation of quantum well, although the conduction band minima does not cross the Fermi level. The grey bands without orbital contributions are shown for the fixed layers of the system which do not have any physical significance. In Fig. 13(b) we have presented the individual orbital contributions of Ta-5d and O-2p orbitals in the system. It is evident that similar to the Type-I heterostructure, the the degeneracy of the t_{2g} subband of Ta-5d orbital is lifted in an identical manner. Moreover, there is a similar inter-orbital crossing of d_{xy} and d_{yz}/d_{xz} bands in this Type-II hetero-interface. In this oxygen-rich interface CFS also plays a crucial role in O-2p orbital splitting. After orbital separation, the valence bands become an admixture of $p_y + p_x$ orbitals and $p_y + p_z$ orbitals, originated from different epitaxial and substrate sub-layers. LRDOS for KO^-/AlO_2^- heterostructure reconfirms the formation of O-rich interface, which presented in Fig. 13(c). Since both the substrate and the epitaxial layers at the interface are made of negatively charged surfaces, the occurrence of hole gas is expected. Similar to the type-I system, the last layer of this heterostructure has also been kept fixed, and the density of states (DOS) of the fixed layer has not been shown here. The states of the conduction subbands do not have much contribution at the heterojunction.

In this section, we have studied Type-II heterostructure in the presence of SOC, and the corresponding band structure is presented in the Fig. 14. The presence of SOC in Type-II system leads to the formation of the Γ_6 and Γ_7 levels. The Γ_6 conduction bands consist of the Ta-5d orbitals, while the valence band consist of O-2p orbitals only. Distinct Γ_6 levels are indicated in the band structure by the numerals 1, 2, 3 etc. Unlike Type-I system, here all the Γ_6 levels show RSO spin splitting, whereas Γ_7 levels has no splitting. This is an oxygen-rich heterojunction, as was previously mentioned, and O-2p orbitals exhibit RSO-splitting in the valence band region. The zoomed in view of the Γ_{6_3} band, which is a combination of the d_{yz}/d_{xz} orbitals, is presented in Fig. 15(a) to demonstrate the k-dependent spin splitting (ΔE_R) (k path from -0.14X to 0.14X). In Fig. 15, we have presented the spin texture corresponding to the Γ_{6_3} band, and the texture clearly shows a modified linear RSO splitting at isoenergy $E=E_f + 0.343$ eV. The inner band maintains a constant spin

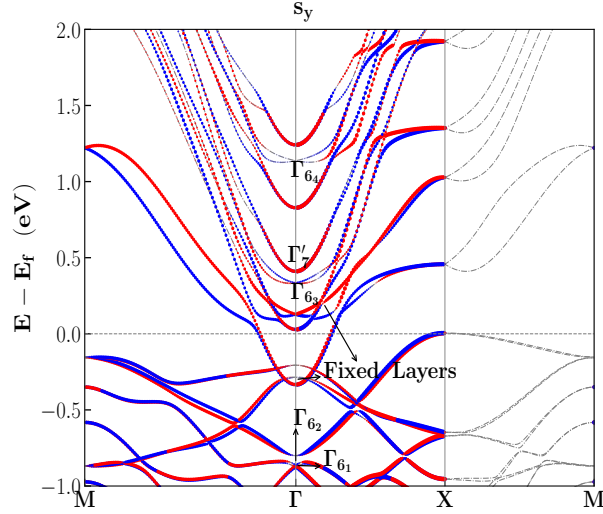


FIG. 14. SOC included band structure along $M - \Gamma - X - M$ contributed by Ta-5d and O-2p orbitals. Red and blue colored circles represent up and down spin polarization along s_y . The circle size represent the weight of the spin.

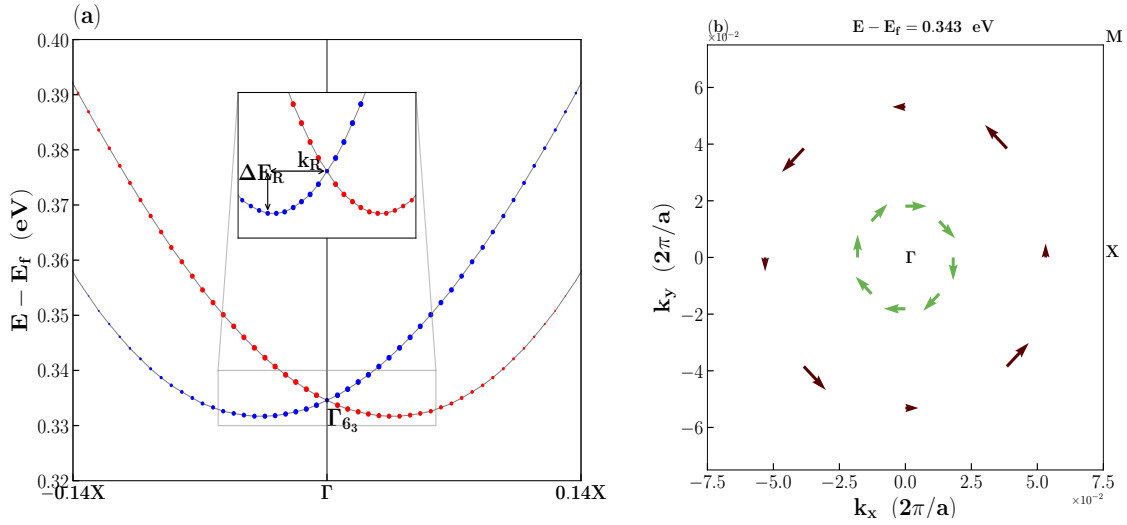


FIG. 15. (a) Spin-split Ta- d_{yz}/d_{xz} band along $-X - \Gamma - X$ symmetry. ΔE_R indicates the maximum energy difference between HS and the extremum of the parabola at k_x , where the maximum linear RSO splitting has been found. (b) Associated spin-textures of Γ_6 band in the $k_x - k_y$ plane at iso-energy $E - E_f = 0.343$ eV. Brown and green colors distinguish between the outer and inner bands with opposite spin orientation.

projection in the $k_x - k_y$ plane, while in the outer band the amplitude of the spin projection periodically changes with momentum. In order to estimate the RSO coupling strength for Type-II system, the DFT band dispersion data is fitted with Eqn. C1. In Table V, the results for all the Γ_6 bands are presented. For both the Γ_{6_1} and Γ_{6_2} bands, linear RSO coupling strength is very strong with $\alpha_{R1} \approx 780 \text{ meV\AA}$ and $\alpha_{R1} \approx 800 \text{ meV\AA}$ respectively. In the conduction band region, up-to within $k_x \lesssim 0.05 \text{ \AA}$, Γ_{6_3} and Γ_{6_4} level shows linear RSO splitting with coupling strength 200 meV\AA and 260 meV\AA respectively.

Fig. 16 is a schematic representation of the possible electronic arrangement for producing

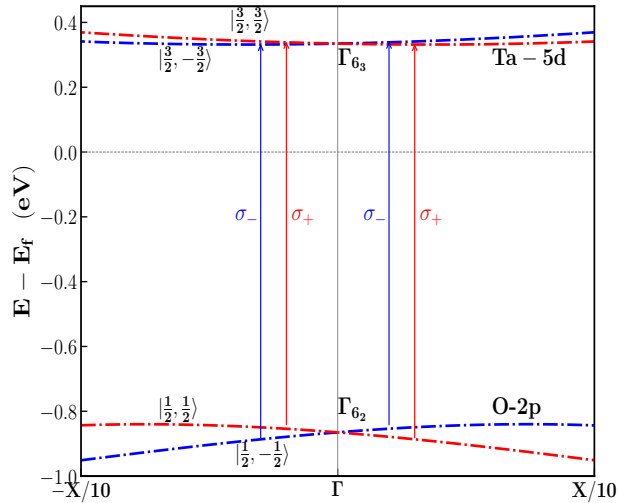


FIG. 16. Schematic representation of circularly polarized photogalvanic effect for Type-II system. σ_+ (red) and σ_- (blue) are the right handed and left handed polarized light. Red and blue arrows show the possible transitions.

circularly polarized photocurrent in the LAO/KTO heterostructure. For the right-handed polarized light (σ_+), the interband transition is possible only for $|j, m_j\rangle = |\frac{1}{2}, \frac{1}{2}\rangle \rightarrow |\frac{3}{2}, \frac{3}{2}\rangle$ and similarly for left handed polarized light (σ_-) the only possible transition is $|j, m_j\rangle = |\frac{1}{2}, -\frac{1}{2}\rangle \rightarrow |\frac{3}{2}, -\frac{3}{2}\rangle$. In the Type-II system, we have shown schematically the transition takes place between Γ_{6_2} and Γ_{6_3} levels which belong to EL-I and SL-X.

1. Fitting for RSO parameter in Type-II heterostructure with fixed substrate layer

TABLE V. The table represents the RSO coupling strength for Type-II system obtained by fitting Eqn. C1 with calculated DFT band dispersion data. Corresponding plots are shown in supplemental material.

Band level	α_{R1}	α_{R3}
	(eVÅ)	(eVÅ ³)
Γ_{6_1}	0.78	-15.3
Γ_{6_2}	0.80	-19.4
Γ_{6_3}	0.20	-3.2
Γ_{6_4}	0.26	-85.4

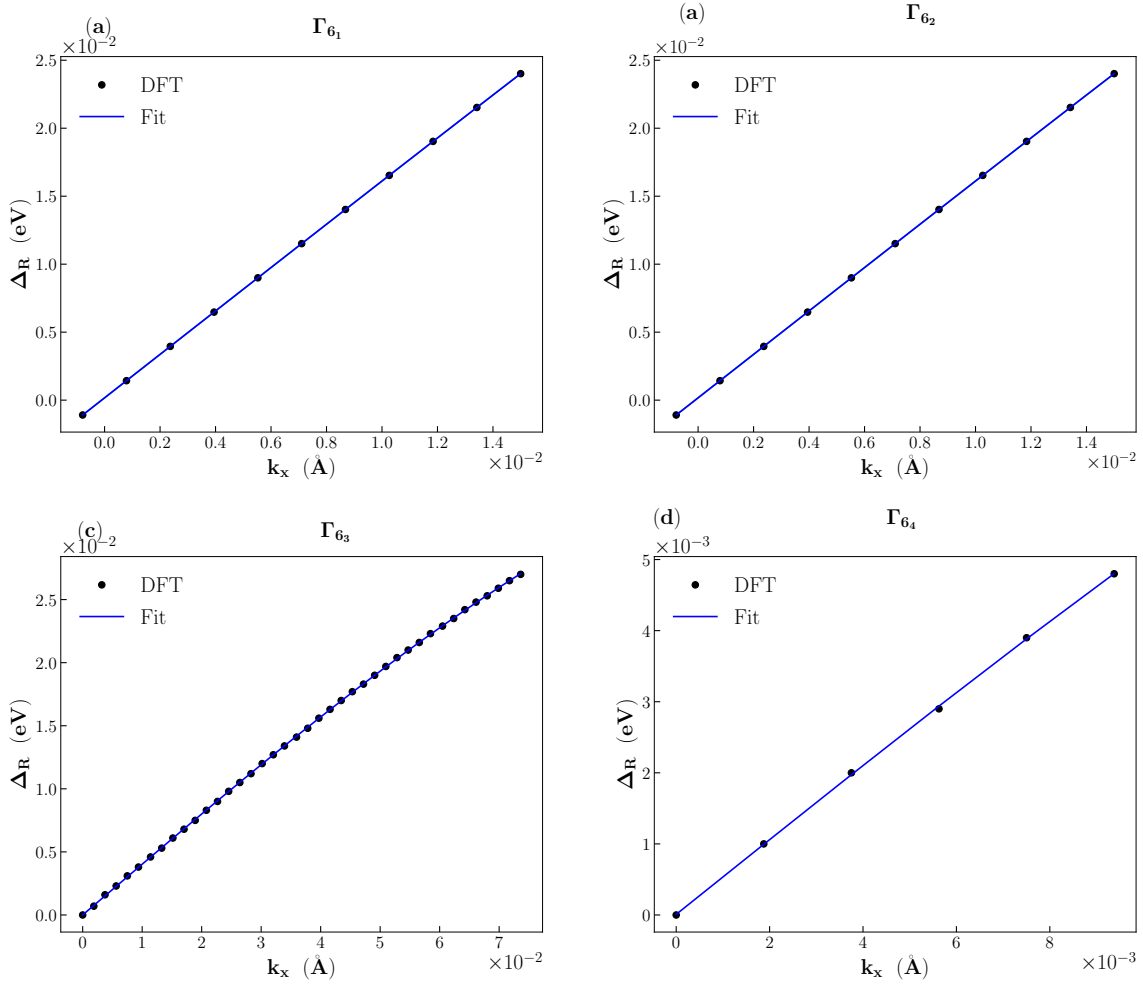


FIG. 17. Hamiltonian fitting by using eqn. C1 for (a) Γ_{6_1} (b) Γ_{6_2} (c) Γ_{6_3} (d) Γ_{6_4} bands